fluids

MDPI

Article

Exploring the Effectiveness of Visualization Techniques for NACA Symmetric Airfoils at Extremely Low Reynolds Numbers

Ángel Antonio Rodríguez-Sevillano [1,*], María Jesús Casati-Calzada [1], Rafael Bardera-Mora [2], Lucía Ballesteros-Grande [1], Lucía Martínez-García-Rodrigo [1], Alejandra López-Cuervo-Alcaraz [1], Jaime Fernández-Antón [1], Juan Carlos Matías-García [2] and Estela Barroso-Barderas [2]

[1] Escuela Técnica Superior de Ingeniería Aeronáutica y del Espacio (ETSIAE), Universidad Politécnica de Madrid (UPM), 28040 Madrid, Spain; mariajesus.casati@upm.es (M.J.C.-C.); lucia.ballesteros.grande@alumnos.upm.es (L.B.-G.); lucia.martinezg@alumnos.upm.es (L.M.-G.-R.); a.lopez-cuervoa@alumnos.upm.es (A.L.-C.-A.); jaime.fernandez.anton@alumnos.upm.es (J.F.-A.)

[2] Instituto Nacional de Técnica Aeroespacial (INTA), Torrejón de Ardoz, 28850 Madrid, Spain; barderar@inta.es (R.B.-M.); matiasgjc@inta.es (J.C.M.-G.); barrosobe@inta.es (E.B.-B.)

* Correspondence: angel.rodriguez.sevillano@upm.es

Abstract: This article aims to highlight the importance of utilizing flow visualization techniques in the preliminary analysis of streamlined and bluff bodies, especially the potential use of visualization with ink in a water channel as a tool for a preliminary approach during fluid mechanics analysis. According to this, the study compares the results obtained using a classical flow visualization technique, ink injection in water, with those obtained through the employment of a laser-based measurement and visualization technique, called PIV, in a low-speed wind tunnel. The article briefly presents both techniques and highlights the importance of flow visualization in the analysis of aerodynamic bodies. This study focuses on flow over NACA airfoils at extremely low Reynolds numbers, which is of great interest for application in extraterrestrial atmospheres, such as on Mars. After obtaining images of the flow streamlines over the NACA 0018 airfoil, the results of both techniques were compared. The results indicated that there was good agreement between the visualization with the water channel and the PIV results, suggesting that the results obtained in the water channel represented a scientifically valid approximation and an essential complement to computational models that require experimental validation.

Keywords: flow visualization; extremely low Reynolds numbers; towing tank; NACA airfoils; PIV

Citation: Rodríguez-Sevillano, Á.A.; Casati-Calzada, M.J.; Bardera-Mora, R.; Ballesteros-Grande, L.; Martínez-García-Rodrigo, L.; López-Cuervo-Alcaraz, A.; Fernández-Antón, J.; Matías-García, J.C.; Barroso-Barderas, E. Exploring the Effectiveness of Visualization Techniques for NACA Symmetric Airfoils at Extremely Low Reynolds Numbers. *Fluids* **2023**, *8*, 207. https://doi.org/10.3390/fluids8070207

Academic Editor: D. Andrew S. Rees

Received: 9 May 2023
Revised: 8 July 2023
Accepted: 9 July 2023
Published: 14 July 2023

1. Introduction

This paper introduces the flow visualization of conventional airfoils, in order to analyze the validation of experimental techniques that are typically used to study airfoils, which is the final aim of this paper. Flow visualization allows, on some occasions, discovering phenomena that would not have been possible to know with point to point measurement techniques such as hot wire anemometry or laser Doppler anemometry [1]. There are several outstanding papers and books that present a rigorous compendium of flow visualization techniques [2–4]. Clayton and Massey [3] reviewed all the principal techniques of flow visualization in water. They took into account the possibility of obtaining quantitative information from these techniques. Dye visualization is one of the easiest to carry out, but it is not so easy to conduct properly. The technique requires the correct selection of the dye class (properties, level of buoyancy, color, etc.) and the proper position of the holes or needles over the surface model. Water tunnels also offer great advantages for research of low Reynolds number aerodynamics accompanied by PIV and have already been used in [5].

Some important concepts that appear in flow visualization are the fluid particle, the trajectory, the fluid streamlines, and streaklines. The fluid particle is an elementary fluid mass that is at a given position at a given time and within which the macroscopic properties remain unchanged. The trajectory is the law that describes its position as a function of time and its initial position. The trajectory equations provide the pathway along which the fluid particle moves. To describe the streaklines of a fluid, it can be imagined that the fluid particles are coated with dye. From the point at which the dye is applied (P), a curve will be marked, called the streakline of P. The streamlines are the lines that are tangent to the local flow velocity at each point. They show how the fluid is moving visually. In steady state, the three lines described above converge into one. Steady state occurs when the fluid quantities that characterize it remain constant over time. This is the case in this paper. For example, in Figure 1 a simplified flow visualization can be observed over a Mars rover prototype.

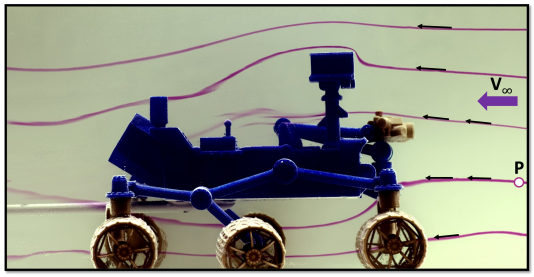

Figure 1. Streamlines (in purple) over a Mars rover.

CFD can be applied for low Reynolds numbers, but the critical point is the presence of laminar regions and the study of the separation point of the transition from laminar to turbulent flow, which cannot be accurately detected and for some Reynolds numbers can lead to incorrect results [6–8]. For that reason, this paper only presents the results of experimental tests.

It is interesting to first understand the flow behavior around a body. Karman vortices will appear and their shape depends on the Reynolds number that is considered [9]. It can be seen in Figure 2 that, at very low Reynolds numbers, below 5, the flow is unseparated. Then, with the increase in the Reynolds number, first a pair of Föppl's vortices appear, second a vortex street; afterwards, there is a transition phase to turbulent, and finally the vortex street reappears in the turbulence region.

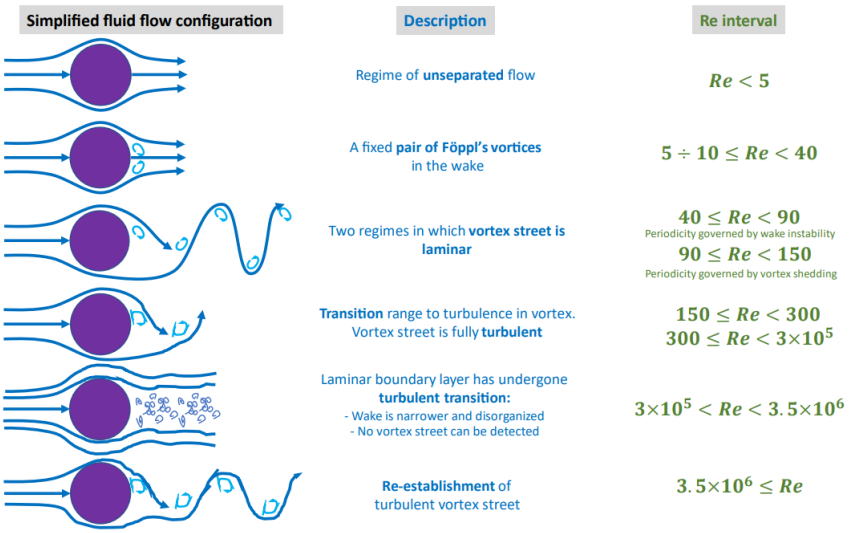

Figure 2. Variation of the Von Karman vortex streets as a function of the Reynolds number, adapted from [9].

Low Reynolds numbers have gained importance in recent years, due to new research paths and recent literature, as cited in [10–12]. One of the primary motivations for studying low Reynolds numbers is their potential use in MAVs (micro air vehicles) in the Martian atmosphere [12–16]. In addition, other applications have been proposed, such as reconnaissance in hostile territories or missions in which human life would be at risk, as mentioned in [17,18]. Technologies for building these MAVs are achievable, as noted in [11]. The martian environment is of particular interest, due to its atmospheric density and temperature, resulting in low Reynolds numbers between 10^3 and 10^5 [12], which justify the Reynolds numbers used in this paper.

The Reynolds number is obtained from the Navier–Stokes equations. These are the general equations that govern the fluid behavior: continuity (Equation (1)), momentum (Equation (2)), and energy (Equation (3)).

$$\frac{\partial \rho}{\partial t} + \nabla \cdot (\rho \vec{v}) = 0 \tag{1}$$

$$\frac{\partial (\rho \vec{v})}{\partial t} + \nabla \cdot (\rho \vec{v} \vec{v}) = \nabla \cdot \left(-pI + \tau'\right) + \rho \vec{f}_m \tag{2}$$

$$\frac{\partial}{\partial t}\left[\rho\left(e + \frac{1}{2}v^2\right)\right] + \nabla \cdot \left[\rho\left(e + \frac{1}{2}v^2\right)\vec{v}\right] = \nabla \cdot \left(-p\vec{v} + \tau' \cdot \vec{v} + k\nabla T\right) + \rho \vec{f}_m \cdot \vec{v} + Q \tag{3}$$

where ρ is the density, $\vec{v}$ is the velocity vector, p is the fluid pressure, I the identity tensor, τ' is the viscous stress tensor, $\vec{f}_m$ is the vector of mass forces, e is the intern energy, $\frac{1}{2}v^2$ is the kinetic energy, k is the coefficient of thermal conductivity, T the temperature, and Q the heat received from outside.

If the non-dimensional forms of these equations are defined, some important non-dimensional numbers appear, such as St (Strouhal), Eu (Euler), Fr (Froude), M (Mach), and Re (Reynolds). According to the main conditions of the experiments, Re is the most relevant number. Then, from the momentum equation the Reynolds number can be obtained by relating the inertial forces term and the viscous forces term. Finally, this can be written as

$$Re = \frac{\rho U l_c}{\mu} = \frac{U l_c}{\nu}, \tag{4}$$

where ρ is the density, U the velocity, l_c the characteristic length, and μ the dynamic viscosity. Sometimes the Reynolds number is expressed using the kinematic viscosity, $\nu = \frac{\mu}{\rho}$. The parameters used for the Reynolds number calculation in each case are shown in Table 1.

Table 1. Estimated Reynolds number for Mars. The velocity was obtained from [9,14,19].

Environment	Velocity (m/s)	Typical Length (m)	Dynamic Viscosity (Ns/m^2)	Density (kg/m^3)	Reynolds Number
Mars	10	0.28	9.82×10^{-6}	1.9×10^{-2}	5500
Ink injection in water	2.7×10^{-2}	0.20	1.00×10^{-3}	10^3	5500
Particle Image Velocimetry in air	2	0.04	1.78×10^{-5}	1.22	5500

Most of the literature, as cited in [10,20,21], indicate that the behavior of an airfoil at low Reynolds numbers features the apparition of a bubble on the trailing edge of the airfoil, which increases with the angle of attack, until it explodes and a stall occurs. Kunz [7] concluded that, for thin airfoils, the stall is more progressive at the beginning, but at a certain angle of attack, the lift coefficient suddenly falls. However, for thick airfoils, the

stall is progressive in all cases. This is the main reason why the authors decided to start this research with thick airfoils.

2. Methods

This section includes an explanation of the experimental methods that were applied to obtain the separation point at different angles of attack, with a description of the equipment used, the airfoil selection, and brief details of the procedures.

The experimental techniques used were as follows:

- Ink injection in water

  Due to their simplicity, low cost, and conceptual clarity, ink injection in water were among the first techniques to be carried out in this field of science. Despite their simplicity, these tests allow the study of several relevant phenomena in fluid mechanics, and although they are purely qualitative and need to be accompanied by various numerical results, these processes provide great consistency to a study. They are generally performed with laminar flow, as turbulence does not allow clear and differentiable fluid patterns to be created. The dye used must be soluble in water, have a controlled density, and have a value very similar to that of water, with a clearly distinguishable color during the test. Another advantage of this procedure compared to those carried out in a wind tunnel is the great simplicity and low cost of the infrastructure. A wind tunnel requires tolerances that are far above the requirements required to build a water channel. Additionally, a water channel can have a laminar flow of water with two large tanks, where the tests with models are performed statically, or it can be a simple water channel, where the model moves through a static fluid with the help of a trolley; that is, a towing tank. The latter prototype was available in the laboratory where the tests for this article were carried out.
  To implement this method, a water channel (water towing tank—WTT) located at the School of Aeronautics and Space Engineering (ETSIAE-UPM) was used. Figure 3 shows a sketch of this channel, with all its measures. The channel (1 in Figure 3) was a rectangular prism made of methacrylate, with dimensions of 3000 mm in length, 720 mm in height, and 420 mm in width, and it maintained a velocity of 0.027 m/s for the experiments (Table 1). The models were connected to the trolley by a mobile structure (3 in Figure 3) that could obtain a three-axis adjustment, allowing them to be placed in the correct orientation for each case.

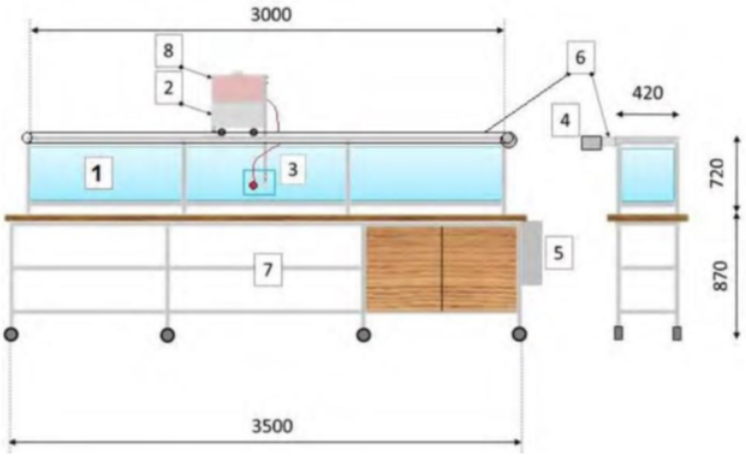

Figure 3. Simplified depiction of the water towing tank, including dimensions in mm and the main elements. The parts in the Figure are: channel (1), trolley (2), airfoil (3), engine (4), engine control box (5), belt (6), storage space (7) and ink reservoir (8).

In order to take pictures during the test, two cameras were used. The lateral images were taken using a AF-S NIKKOR 18–140 mm VR, using a steady position (with a static and robust tripod). The tripod was located at the same point for every test, taking the pictures when the model arrived at that part of the channel.

- Particle Image Velocity in air

  Particle image velocimetry (PIV) is a technique dedicated to measuring the flow velocity field [22]. It was introduced in the 1990s, and it continues to be developed. It typically combines a double-pulsed laser with a specialized digital camera with a synchronization system. It is considered an appropriate method for indoor airflow investigations, since it is a non-intrusive technique, but it has inconveniences [23]. If the airfoil is not transparent, there is a light-obstruction problem, because the optical paths are blocked; however, if the airfoil is transparent, there can be distortion of the particles' images. The PIV technique is based on measuring the velocity of tracer particles [24,25] that are transported by the fluid. To achieve this, a pulsed laser is used to illuminate the plane of the fluid being studied, which is generated using a light sheet and suitable optics. The particles are illuminated twice with a laser light sheet. With the correlation of these two pictures, the particle displacement can be calculated. With the following equation, the velocity can be obtained:

$$\vec{u}(\vec{X},t) = \frac{\Delta\vec{X}(\vec{X},t)}{\Delta t} \tag{5}$$

Finally, a visual layout of the PIV is shown in the following Figure 4:

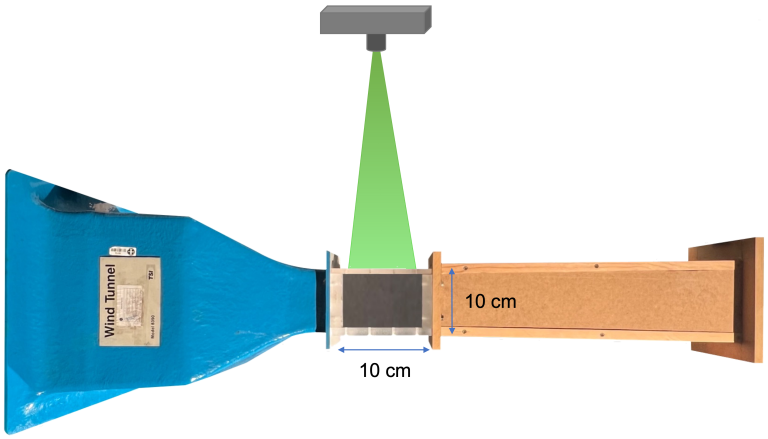

Figure 4. PIV light shot on the test section.

The experiments with this method were carried out at the Experimental Aerodynamics Laboratory of the National Institute for Aerospace Technology (INTA) with a modified wind tunnel based on a commercial wind tunnel (TSI model 8390) [26]. This is an open-circuit wind tunnel with a closed test section with a square cross-section of 100×100 mm^2, whose acrylic walls allow visual access. In its original version, the tunnel could reach a speed of 45 m/s. However, the tunnel used was a modification of the original version, aimed at obtaining very low air speeds and low turbulence conditions.

The modified tunnel (LSWT) was made up of a new wooden DM diffuser, to properly accommodate the new fan, which offered a lower pressure increase due to its lower speed, allowing the generation of very low Reynolds numbers.

The following Figure 5 shows the modified wind tunnel in which all the tests were carried out.

Figure 5. Main view of the low speed wind tunnel.

The study in the low speed wind tunnel (LSWT) was carried out using a commercial 2D-PIV system from TSI Inc. (Thermo Systems, Incorporated-USA) and the licensed processing software INSIGHT 3G. The illumination was based on two Nd:YAG (Neodymium: Yttrium Alluminium Garnet) pulsed lasers that delivered a maximum energy of 190 mJoule/pulse and a CCD camera with frame-straddling.

The airfoils tested at both facilities were NACA symmetrical airfoils [27]. NACA airfoils have been widely studied, mainly in the atmospheric flight range (10^5–10^7). For extremely low Reynolds numbers, they have been studied for use in drones and for use in fixed-wing and rotary-wing vehicles on Mars, as we have seen in literature references [12–16]. The authors have been developing experimental studies with a water channel with NACA airfoils such as 0006, 0010, 0012, 0016, 0018, 0024, and 0032, among others. Three-dimensional printing is a key tool for manufacturing precise and high-quality aerodynamic models [28]. It allows for rapid manufacturing of prototypes, which accelerates the design and testing process [29].The tested aerodynamic airfoils were manufactured using PLA (polylactic acid), a biodegradable polymer. The equipment used for manufacturing was an Ultimaker 3S 3D printer, and the prototypes were designed using 3D generation modeling software (CATIA, Dassault Systèmes). Figure 6b,c show the results of the printing process.

(**a**) (**b**) (**c**)

Figure 6. Details of the prototypes manufactured using 3D printing. (**a**) Placing the model on the printer with CURA software. (**b**) Prototype tested at LSWT. (**c**) Prototype tested at WTT, showing the holes along the leading edge.

To compare the results obtained in the hydrodynamic channel with those obtained in the low-speed wind channel, only the NACA 0018 airfoil was used. Additionally, there have already been studies with this airfoil in a water channel, which will be detailed later. The main characteristics of the airfoils for the wind tunnel and water channel can be seen in Table 2. It should be noted that, although the NACA 0018 is a symmetric airfoil, it has been selected for use in some applications in the Martian environment, as cited in [13].

Table 2. Characteristics of the NACA 0018 airfoil prototypes tested in the water channel (water towing tank, WTT) and in the low speed wind tunnel (LSWT).

Testing	Chord Length (mm)	Wingspan (mm)	Material
Water channel	200	250	PLA (Polylactic acid)
Wind tunnel	40	100	PLA (Polylactic acid)

To conclude this section, the last comment to be made is about the testing procedure:

- Water Towing Tank (WTT)

  To test the airfoil in the water channel, the model was assembled by connecting the distribution system of tubes to the exit hole of the Mariotte Bottle and to the tubes attached to the trailing edge of the airfoil. Two methacrylate side walls were screwed to the sides of the airfoil, to minimize the 3D effects of the flow, and the airfoil was fastened to the trailing edge support arm (Figure 7). The ink distribution ducts were vented by injecting water into the circuit, until it came out of all the leading edge holes, and the main duct was quickly connected to the ink outlet. After the remaining air was removed, the channel was filled and the airfoil was submerged.

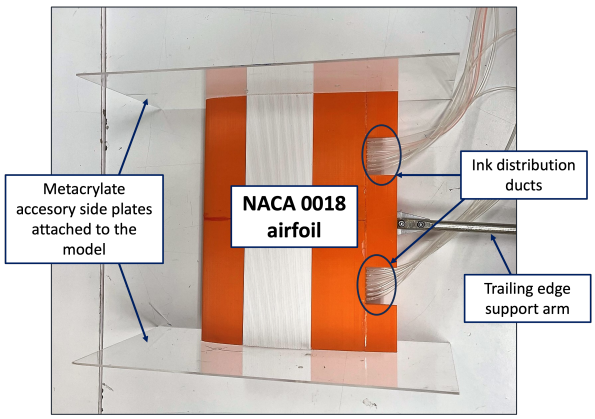

Figure 7. Detail of the prototype with attached side walls, distribution tubes, and trailing edge support arm.

  The camera was placed to capture the flow visualization. The angle of attack of the airfoil was set using a level, and the profile was brought to the center area of the channel. The Nikon lens was focused on the leading edge, and the test began after allowing 5 min for the water to calm down. The main features of the pictures were a focal distance of 18 mm, f/3.5, exposure time 1/20 s; for all experiments, due to the extremely low speed of the trolley, it was possible to obtain more than 30 images in a short period of time; that is, in one minute. Finally, tests were carried out at a Reynolds number of 5500 (Table 1) for angles of attack from 0° to 10°.

- Low Speed Wind Tunnel (LSWT)

  In this case, the model was placed (Figure 8b) using a rod that went from left to right in 25% of the chord (c/4). The next step was to prepare the tracer particles. With oil, there was a spray that threw the particles, but with water, the humidifiers were placed near the entrance of the tunnel (Figure 8a). A camera (PowerView 4M Plus or Iphone 13 Pro Max) was placed on the side of the tunnel to capture the visualization of the flow. The picture properties were a focal distance of 5.7 mm, f/1.5, and exposure time 1/436 s. The angle of attack was changed before the laser started up, from 0° to 12°, and the experiments were conducted with a Re = 5500.

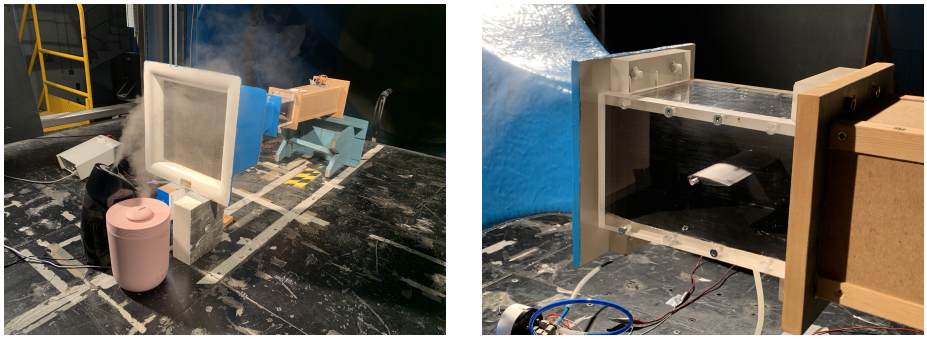

(**a**) (**b**)

Figure 8. Details of the low speed wind tunnel testing (LSWT) procedure. (**a**) Entrance of the LSWT. (**b**) NACA airfoil placed in the center of the test section.

3. Results

The following subsections include the results obtained after testing the NACA 0018 airfoil in the water channel and in the wind tunnel.

3.1. Water Towing Tank (WTT) Experiments

The NACA 0018 airfoil was tested at different angles of attack (α) (0, 2, 4, 6, 8, and 10°). For each of these, a lateral view of the experiment is presented. The evolution of the boundary layer separation point will be commented on below.

For the first case (Figure 9), it can be observed that the flow on the upper surface separated at x/c = 61% (Figure 9a), despite being at zero angle of attack. In addition, the boundary layer separated in a laminar regime (Figure 9b), without generating turbulence.

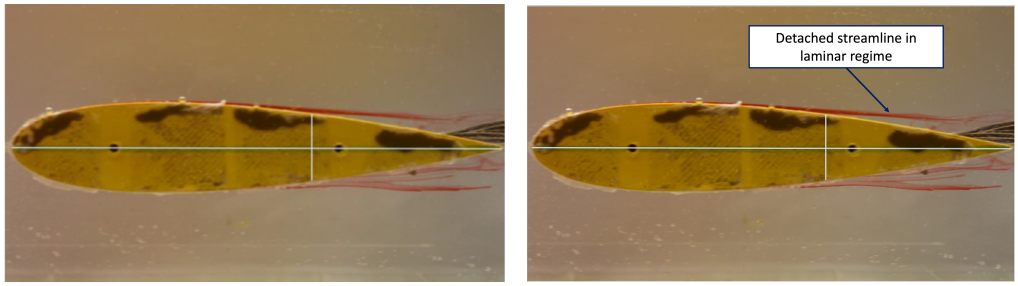

(**a**) (**b**)

Figure 9. NACA 0018 WTT visualization at $\alpha = 0°$. (**a**) Streamline over the upper surface of the airfoil, at $\alpha = 0°$. (**b**) Laminar regime after after the detachment at $\alpha = 0°$.

As the angle of attack was increased to 2° (Figure 10), an advancement of the point of flow separation located at x/c = 50% was observed (Figure 10a). Likewise, despite still separating in a laminar regime, it can be seen how the streamlines began to curve slightly at the trailing edge (Figure 10b).

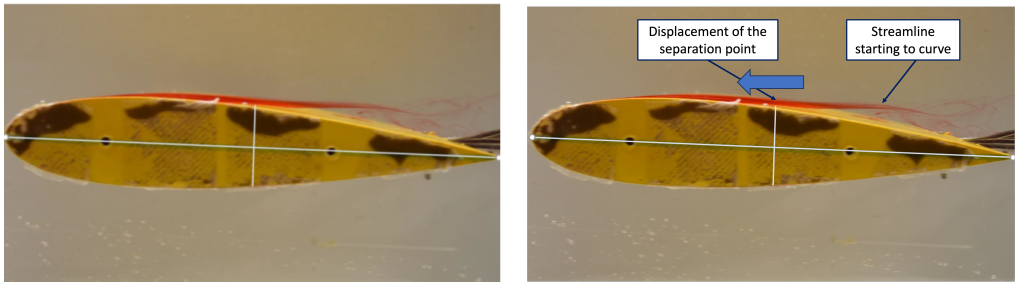

(**a**) (**b**)

Figure 10. NACA 0018 WTT visualization at $\alpha = 2°$. (**a**) Streamline over the upper surface of the airfoil, at $\alpha = 2°$. (**b**) Curving detail close to the trailing edge, at $\alpha = 2°$.

Continuing to increase the angle of attack, at $\alpha = 4°$ (Figure 11), the point of separation approached the leading edge, until it was located at x/c = 44% (Figure 11a). As in the previous case, the boundary layer began to wave upon reaching the trailing edge (Figure 11b).

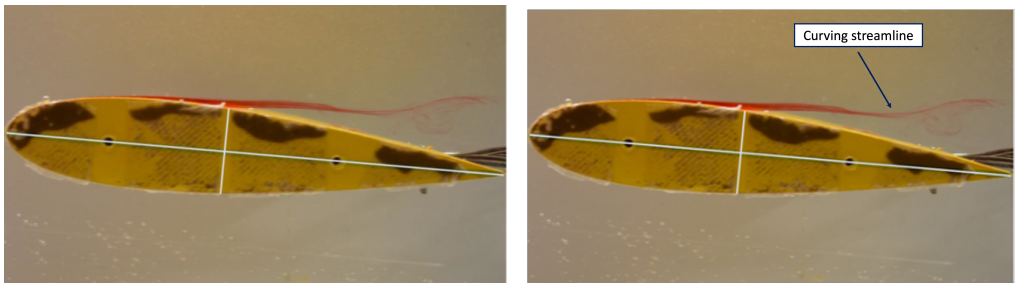

(**a**) (**b**)

Figure 11. NACA 0018 WTT visualization at $\alpha = 4°$. (**a**) Streamline over the upper surface of the airfoil, at $\alpha = 4°$. (**b**) Curving streamline around the trailing edge, at $\alpha = 4°$.

In this case, at $\alpha = 6°$ (Figure 12), the small variation between the previous image and this one, in which the flow separated at x/c = 43% (Figure 12a), is striking. However, the waviness of the separated flow was clearly more pronounced at this angle of attack (Figure 12b), with turbulence beginning to appear. In addition, it was at this angle of attack that thickening of the boundary layer could be perceived, denoting the transition to a turbulent regime.

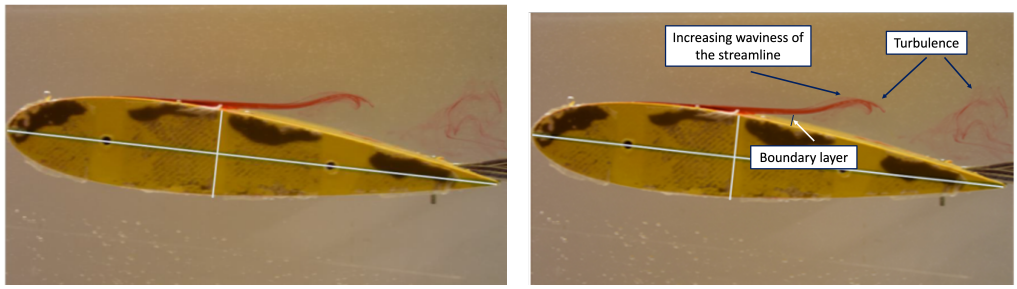

(**a**) (**b**)

Figure 12. NACA 0018 WTT visualization at $\alpha = 6°$. (**a**) Streamline over the upper surface of the airfoil, at $\alpha = 6°$. (**b**) Relevant details of the flow, at $\alpha = 6°$.

Increasing the angle of attack to $\alpha = 8°$ (Figure 13), separation occurred at x/c = 40% (Figure 13a) and it can be appreciated how the separated flow curved due to turbulence (Figure 13b).

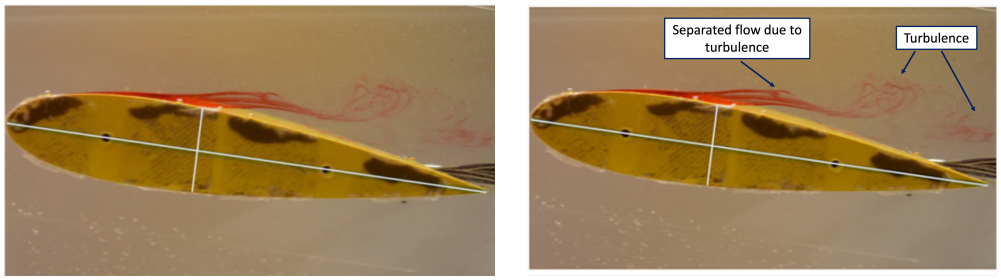

(**a**) (**b**)

Figure 13. NACA 0018 WTT visualization at $\alpha = 8°$. (**a**) Streamline over the upper surface of the airfoil, at $\alpha = 8°$. (**b**) Separation flow condition of the flow, at $\alpha = 8°$.

Finally, at $\alpha = 10°$ (Figure 14) the boundary layer separation occurred at x/c = 34% (Figure 14a) and maintained the tendency for the onset of turbulence (Figure 14b) as in the previous Figures 13b and 12b.

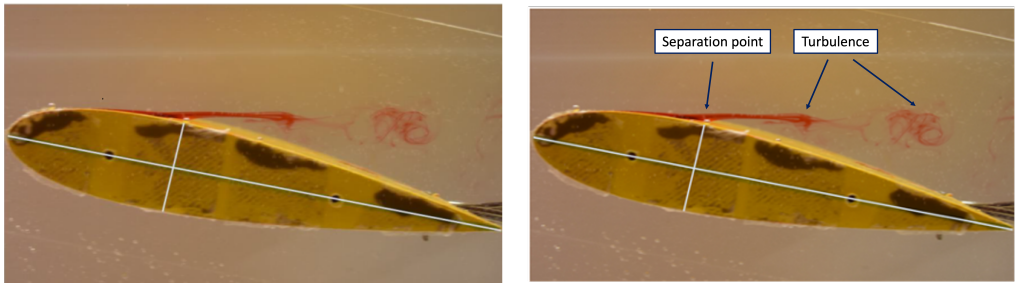

(**a**) (**b**)

Figure 14. NACA 0018 WTT visualization at $\alpha = 10°$. (**a**) Streamline over the upper surface of the airfoil, at $\alpha = 10°$. (**b**) Separation point and turbulence zones, at $\alpha = 10°$.

3.2. Low Speed Wind Tunnel (LSWT) Experiments

In this subsection, the wind tunnel results will be explained. As previously mentioned, two different tracer particles were used: oil and water. Figures 15a–18a show the visualized airfoil at angles of attack of 0, 4, 8, and 12° with oil tracer particles. Figures 15b–18b show the same airfoil and angles of attack but with water tracer particles. To obtain the separation point, both particles techniques are useful, to compare to each other. It should be noted that, for some angles of attack, the differences were quite significant.

Figure 15 shows that the separation point at $\alpha = 0°$ from the leading edge was at x/c = 76.3% for oil particles, but for water particles it was at x/c = 87.5%. It can be seen that, in both cases, the flow was disturbed and appeared as vorticity after the trailing edge.

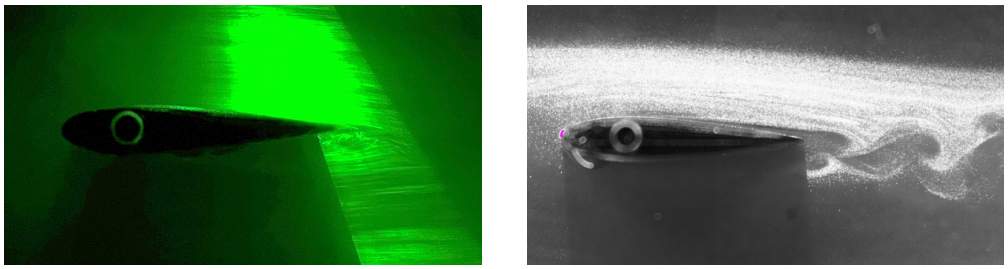

(**a**) (**b**)

Figure 15. NACA 0018 LSWT visualization at $\alpha = 0°$. (**a**) Oil tracer particle technique. (**b**) Water tracer particle technique.

The separation point (Figures 16) at $\alpha = 4°$ was at x/c = 59.6% for oil particles and x/c = 45.5% for water particles. The flow was modified near the trailing edge, and the vortices were more accentuated.

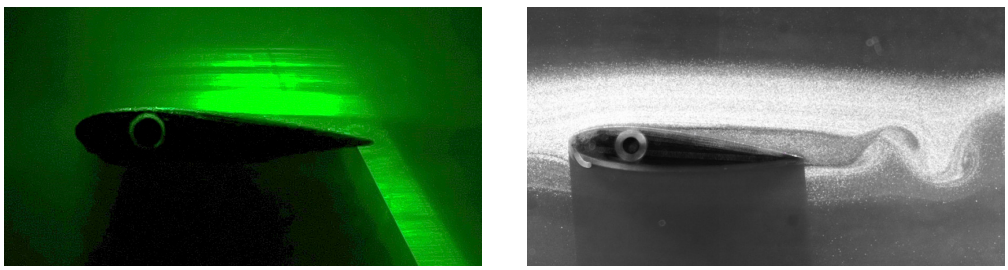

(**a**) (**b**)

Figure 16. NACA 0018 LSWT visualization at $\alpha = 4°$. (**a**) Oil tracer particle technique. (**b**) Water tracer particle technique.

Figure 17 shows that for $\alpha = 8^\circ$ a recirculation bubble appeared. The separation point was at x/c = 51.5% for oil particles and at x/c = 22.2% for water particles. In Figure 17a,b the turbulence increased substantially and the separation points of the different particles were further apart.

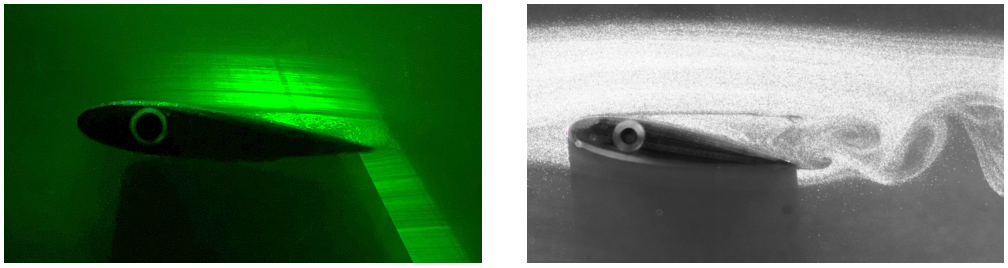

(**a**) (**b**)

Figure 17. NACA 0018 LSWT visualization at $\alpha = 8^\circ$. (**a**) Oil tracer particle technique. (**b**) Water tracer particle technique.

As can be seen in Figure 18, at 12° the turbulence was more intense than with 8°, the difference between the separation points was more pronounced and the recirculation bubble increased. For oil particles, the separation point was at x/c = 42.5% and for water particles this was x/c = 11.1%. This cannot be compared with the water towing tank results, but it was interesting to see the flow evolution in a low speed wind tunnel.

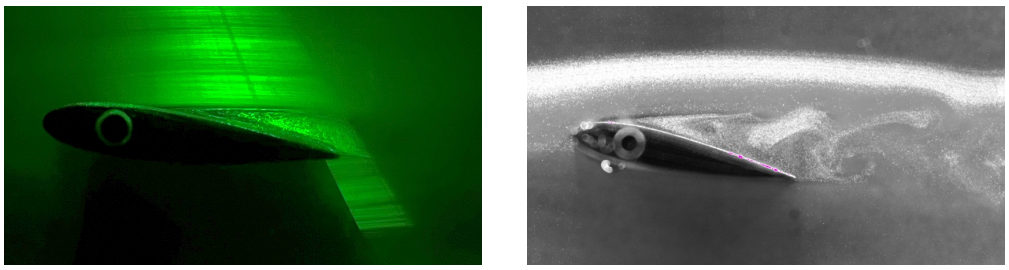

(**a**) (**b**)

Figure 18. NACA 0018 LSWT visualization at $\alpha = 12^\circ$. (**a**) Oil tracer particle technique.(**b**) Water tracer particle technique.

According to these results obtained with different techniques in the low speed wind tunnel (LSWT), we can confirm, on the one hand, that the oil tracer particle technique is appropriate for studying the recirculation bubble. Based on Figure 19, it is possible to characterize the dimensions and streamlines of the recirculation bubble.

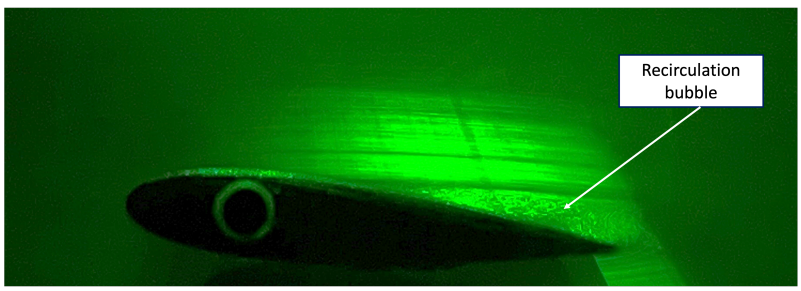

Figure 19. Image of the recirculation bubble at $\alpha = 8^\circ$ obtained with the oil tracer particle technique in the LSWT.

On the other hand, with the water tracer particle technique, it is possible to carry out a proper visualization of the flow region dominated by vortices. In Figure 20, it is possible to study the structure of the vortex street, the frequency shedding, and the distance between them.

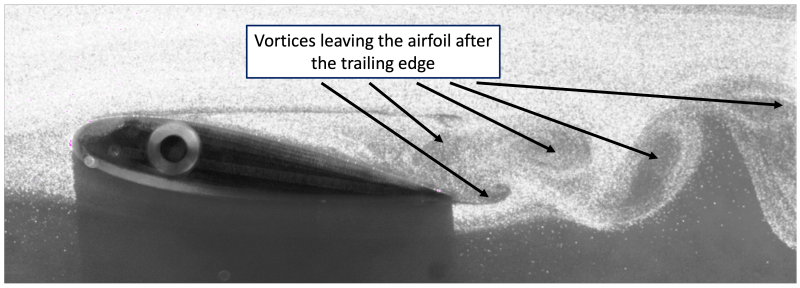

Figure 20. Vortices structure after the airfoil at $\alpha = 8°$, obtained with the water tracer particle technique in the LSWT.

Finally, the streamline map and the non-dimensional velocity contours were calculated for the different angles of attack studied (Figure 21) using the PIV tests. This technique is appropriate for studying in depth and for determining precise values of the velocity contours and streamlines, and it is therefore suitable for determining the point of flow separation. In this case, the separation points were x/c = 72.7%, 41.8%, 36.4%, and 30.2% for $\alpha = 0°, 4°, 8°, 12°$, respectively. We could observe the same pattern of the separation point as in the previous tests; that is, the displacement forward from the trailing edge to the leading edge.

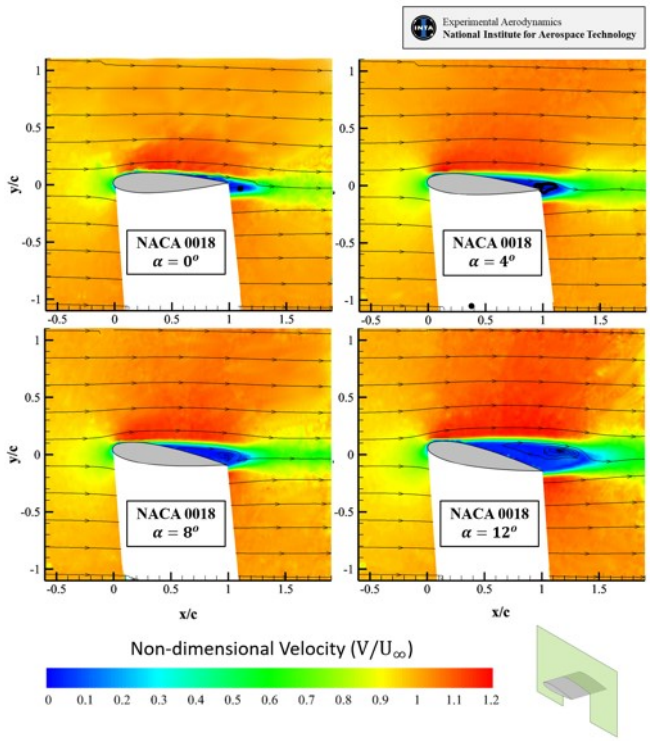

Figure 21. Non-dimensional velocity contours and streamlines of the flow over NACA 0018 with the PIV technique.

Using the results of the different methods, a comparison could be made. The Reynolds numbers in all the experiments were conserved. According to the values expressed in Table 1, there were several geometrical differences between the prototypes; for example, the wing aspect ratio ($AR = \frac{model\ span^2}{area}$) was not exactly the same (due to geometrical constraints). According to the previous explanations and based on dynamic similarity conditions from Equation (2), the behavior of the flow had the same dynamic conditions in all experiments, obviously, but not all the techniques had the capability to properly show the same flow properties.As stated above, the three visualization techniques (WTT, LSWT

water tracer and LSWT oil tracer particles) and PIV technique were capable of illustrating different features of the flow, such as the evolution of the separation point, description of the detached region, vortices structure, recirculation bubble, and the onset of turbulence. The wind tunnel results also differed depending on the tracer particle used. This happened because of the size of the water particles. The size of the water particles was approximately 10 µm, which made the inertial effects important. This implies that the trajectory of the particles did not represent the streamlines, so the separation points cannot be extracted exactly from the figures. Thus, despite being an appropriate technique for studying the vortex structure downstream of the airfoil (as shown in Figure 20), it is clear that it is not suitable for determining the evolution of the separation point at such extremely low Reynolds numbers.

In Figure 22, it can be seen that the separation point had the same evolution for all techniques. Excluding the wind tunnel water particle technique (due to the size of the particles), the other techniques exhibited a similar behavior. Since the objective of visualization was to obtain a preliminary analysis of flow characteristics, this objective was met.

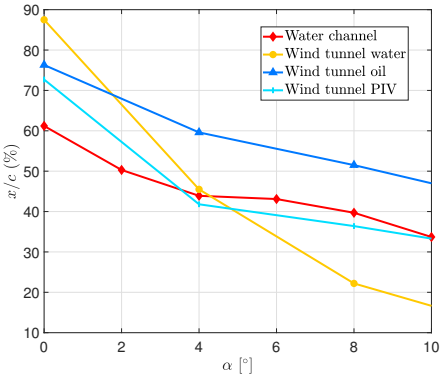

Figure 22. Comparison of the separation point position (x/c) as a function of the angle of attack (α) for the four visualization techniques analyzed.

To more accurately focus the analysis of the results obtained with all visualization methods, the error values for each technique are included in Figure 23. For this purpose, the error (ϵ) is defined according to Equation (6). The PIV technique was considered as a reference for the others, as it was used to determine the local fluid velocity, with an accuracy of around 1%.

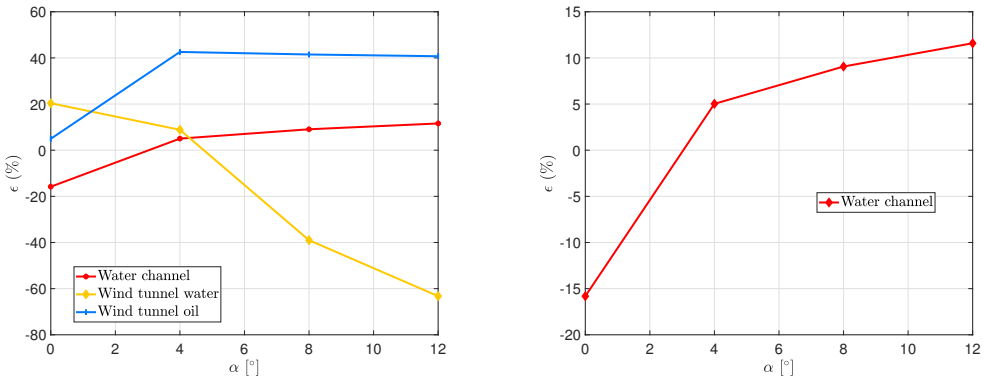

(**a**) (**b**)

Figure 23. Comparison of the error (ϵ) in separation point position (x/c) as a function of the angle of attack (α) for the three visualization techniques analyzed. The error ϵ was defined according to PIV (x/c) values as a reference. (**a**) Error (ϵ) for the three visualization techniques. (**b**) Error (ϵ) for the WTT visualization technique.

$$\epsilon = \frac{(x/c)_{technique_i} - (x/c)_{PIV}}{(x/c)_{PIV}} \quad (6)$$

Figure 23a shows the separation point results for each technique; these results were derived from Figure 23 but in terms of the error defined by Equation (6). It can be observed that the technique with the worst results was the water tracer particle technique, a conclusion already explained. Furthermore, Figure 23b focuses solely on displaying the error results of the ink-in-water visualization technique (WTT), which was the main objective of this article. It is true that the obtained error fell within the range of $[-15\% \div 10\%]$, but it should be noted that this is a qualitative technique for preliminary analysis. Therefore, it is considered as meeting the requirements.

4. Conclusions

The aim of this article was to demonstrate the advantages of flow visualization techniques as a preliminary tool for flow analysis. In particular, it aimed to corroborate the usefulness of water visualization in a towing tank (an economically accessible technique) compared to other techniques that require large financial investments. These techniques, based on laser technology, require significant financial investment and a high qualification level and training of personnel in the use of the equipment. In this case, this study focused on determining the flow separation point on a NACA 0018 airfoil at an extremely low Reynolds number of Re = 5500. Throughout the article, the characteristics of the equipment used, both the water channel (WTT) and the low-speed wind tunnel (LSWT), were presented. In addition, the testing procedure with both equipment types was briefly described. On the one hand, this consisted of injecting ink into water, and on the other hand, visualizing with water and oil tracers in a wind tunnel. Once the equipment and testing procedure were described, the obtained images with each technique were analyzed, commenting on the evolution of the separation point of the flow in each case.

Once the results were obtained, they were all presented together (Figure 22), concluding that, except for the case of visualization in the wind tunnel with oil tracers, the results maintained the same tendency. Finally, to give greater validity to the results, they were compared with a high-quality experimental technique in terms of error (ϵ), the particle image velocimetry technique (PIV); although this technique undoubtedly has a very high cost.The results are included in Figure 23 .

The main conclusions presented were as follows:

- Not all visualization techniques have the ability to visualize and explain in detail phenomena such as the flow separation point, boundary layer thickness, recirculation bubbles, vortices downstream of the airfoil, and the onset of turbulence;
- Oil tracer particle visualization in a wind tunnel allows a proper analysis of the recirculation bubble (Figure 19);
- Water particle visualization in a wind tunnel allows easier visualization of vorticity (Figure 20), although it does not follow the same trend as the other two techniques, due to the particle size argument explained;
- The PIV technique is suitable for reliable velocity mapping with a small error (Figure 21);
- The water visualization technique (WTT) shows a very similar trend to PIV (Figure 23b), ensuring the validity of the results, although it may not achieve the same level of accuracy. This validates the results obtained in the water channel, which represents the lowest equipment costs among the techniques.

All of these factors allowed us to validate the final results. Therefore, we can conclude that the water visualization technique (WTT) met the expected requirements.

Author Contributions: Conceptualization, Á.A.R.-S., M.J.C.-C. and R.B.-M.; Methodology, Á.A.R.-S., M.J.C.-C., R.B.-M., L.B.-G., L.M.-G.-R., A.L.-C.-A., J.F.-A., J.C.M.-G. and E.B.-B.; Software, M.J.C.-C., R.B.-M., L.B.-G., L.M.-G.-R., A.L.-C.-A., J.F.-A., J.C.M.-G. and E.B.-B.; Validation, Á.A.R.-S., R.B.-M., L.B.-G., L.M.-G.-R., A.L.-C.-A., J.F.-A., J.C.M.-G. and E.B.-B.; Formal Analysis, Á.A.R.-S., R.B.-M., J.C.M.-G. and E.B.-B.; Investigation, R.B.-M., L.B.-G., L.M.-G.-R., A.L.-C.-A., J.F.-A., J.C.M.-G. and E.B.-B.; Resources, Á.A.R.-S., M.J.C.-C. and R.B.-M.; Data Curation, Á.A.R.-S., M.J.C.-C., R.B.-M., L.B.-G., L.M.-G.-R., A.L.-C.-A., J.F.-A., J.C.M.-G. and E.B.-B.; Writing—Original Draft Preparation, Á.A.R.-S., M.J.C.-C., L.B.-G., L.M.-G.-R. and A.L.-C.-A.; Writing—Review and Editing, Á.A.R.-S., M.J.C.-C., R.B.-M., L.B.-G., L.M.-G.-R., A.L.-C.-A., J.F.-A., J.C.M.-G. and E.B.-B.; Visualization, Á.A.R.-S., M.J.C.-C., R.B.-M., L.B.-G., L.M.-G.-R., A.L.-C.-A., J.F.-A., J.C.M.-G. and E.B.-B.; Supervision, Á.A.R.-S., M.J.C.-C. and R.B.-M. All authors have read and agreed to the published version of the manuscript.

Funding: This research received no external funding.

Data Availability Statement: Not applicable.

Conflicts of Interest: The authors declare no conflict of interest.

Abbreviations

The following abbreviations are used in this manuscript:

LSWT	Low Speed Wind Tunnel
MAVs	Micro Air Vehicles
NACA	National Advisory Committee for Aeronautics
PIV	Particle Image Velocimetry
WTT	Water Towing Tank

References

1. Barcala-Montejano, M.A.; Rodríguez-Sevillano, A.A.; Delgado-Obrero, C. Visualization in a water channel as a preliminary design tool. In Proceedings of the 5th European Conference for Aeronautics and Space Sciences (EUCASS), Munchen, Germany, 1–5 July 2013.
2. Tietjens, O.K.G.; Prandtl, L. *Applied Hydro-and Aeromechanics: Based on Lectures of L. Prandtl*; Courier Dover Publications: Mineola, NY, USA, 1957; Volume 2.
3. Clayton, B.R.; Massey, B.S. Flow visualization in water: A review of techniques. *J. Sci. Instruments* **1967**, *44*, 2. [CrossRef]
4. Werle, H. Hydrodynamic flow visualization. *J. Annu. Rev. Fluid Mech.* **1973**, *5*, 361–386. [CrossRef]
5. Gursul, I.; Taylor, G.; Wooding, C.L. Vortex flows over fixed-wing micro air vehicles. *Am. Inst. Aeronaut. Astronaut.* **2002**.
6. Ballesteros Grande, L.; Martínez García-Rodrigo, L.; Cervigón Corraliza, S.; Eusa López de Murillas, P.; Astudillo Andrés, A.; Casati Calzada, M.J.; Rodríguez Sevillano, A.A. Entrada en pérdida de perfiles NACA a números de Reynolds extremadamente bajos: La aerodinámica en Marte. In Proceedings of the I Semana Interdisciplinar del Espacio y IV Congreso de Ingeniería Espacial, 20–24 June 2022. Available online: https://www.eiecongress.com/programa-completo (accessed on 9 May 2023).
7. Kunz, P.J. *Aerodynamics and Design for Ultra-Low Reynolds Number Flight*; Stanford University: Stanford, CA, USA, 2003.
8. Crivellini, A.; D'Alessandro, V.; Di Benedetto, D.; Montelpare, S.; Ricci, R. Study of laminar separation bubble on low Reynolds number operating airfoils: RANS modelling by means of an high-accuracy solver and experimental verification. *J. Phys. Conf. Ser.* **2014**, *501*, 12024. [CrossRef]
9. Rodríguez-Sevillano, A.A.; Casati-Calzada, M.J.; Bardera-Mora, R.; Feliz-Huidobro, A.; Calle-González, C.; Fernández-Antón, J. Flow Study on the Anemometers of the Perseverance Based on Towing Tank Visualization. *Appl. Mech.* **2022**, *3*, 1385–1398. [CrossRef]
10. Mateescu, D.; Abdo, M. Aerodynamic analysis of airfoils at very low Reynolds numbers. In Proceedings of the 42nd AIAA Aerospace Sciences Meeting and Exhibit, Reno, NV, USA, 5–8 January 2004. Available online: https://arc.aiaa.org/doi/abs/10.2514/6.2004-1053 (accessed on 9 May 2023).
11. Kunz, P.J.; Kroo, I.M. *Analysis, Design, and Testing of Airfoils for Use at Ultra Low Reynolds Numbers*; American Institute of Aeronautics and Astronautics, Inc.: Reston, VA, USA, 2001.
12. Koning, W.J.F.; Romander, E.A.; Johnson, W. Low Reynolds Number Airfoil Evaluation for the Mars Helicopter Rotor. In Proceedings of the AHS International 74th Annual Forum & Technology Display, Phoenix, AZ, USA, 15–17 May2018.
13. Koning, W.J.F.; Johnson, W. Improved Mars Helicopter Aerodynamic Rotor Model for Comprehensive Analyses. *AIAA J.* **2019**, *57*, 3969–3979. [CrossRef]
14. Koning, W.J.F. Airfoil Selection for Mars Rotor Applications. U.S. Patent No. NASA/CR—2019–220236, July 2019.
15. Johnson, W.; Withrow-Maser, S.; Young, L.; Malpica, C.; Koning W.J.F.; Kuang, W.; Fehler, M.; Tuano, A.; Chan, A. Mars Science Helicopter Conceptual Design. U.S. Patent No. NASA/TM—2020–220485, March 2020.

16. Durgesh, V.; Johari, H.; Garcia, E. Aerodynamic behavior and flow visualization on canonical NACA airfoils at low Reynolds number. *Vis. Soc. Jpn.* **2023**. [CrossRef]
17. Winslow, J.; Otsuka, H.; Govindarajan, B.; Chopra, I. Basic Understanding of Airfoil Characteristics at Low Reynolds Numbers (10^4–10^5). *J. Aircr.* **2018**, *55*, 1050–1061. [CrossRef]
18. Sun, Q.; Boyd, I.D. *Flat-Plate Aerodynamics at Very Low Reynolds Number*; Cambridge University Press: Cambridge, UK, 2003.
19. Bardera, R.; Garcia-Magariño, A.; Sor, S.; Urdiales, M. Mars 2020 Rover Influence on Wind Measurements at Low Reynolds Number. *J. Spacecr. Rocket.* **2019**, *56*, 1107–1113. [CrossRef]
20. Mahbub Alam, M.; Zhou, Y.; Yang, H.X.; Guo, H.; Mi, J. *The Ultra-Low Reynolds Number Airfoil Wake*; Springer: Berlin/Heidelberg, Germany, 2009.
21. Samson, A.; Sarkar, S. An experimental investigation of a laminar separation bubble on the leading edge of a modelled aerofoil for different Reynolds number. *J. Mech. Eng. Sci.* **2015**, *230*, 2208–2224. [CrossRef]
22. Persoons, T. Chapter Two—Measuring flow velocity and turbulence fields in thermal sciences using particle image velocimetry: A best practice guide. *Adv. Heat Transf.* **2022**, *54*, 37–87. [CrossRef]
23. Goodfellow, H.; Wang, Y. *Industrial Ventilation Design Guidebook*; Elsevier: Amsterdam, The Netherlands, 2021.
24. Lindken, R.; Burgmann, S. *Laser-Optical Methods for Transport Studies in Low Temperature Fuel Cells*; Elsevier: Amsterdam, The Netherlands, 2012.
25. Rodi, W.; Laurence, D. *Engineering Turbulence Modelling and Experiments 4*; Elsevier: Amsterdam, The Netherlands, 1999.
26. TSI Inc. *Model 8390 Bench Top Wind Tunnel P/N 1980004 Rev C*; TSI Inc.: Saint Paul, MN, USA, 1989.
27. Abbot, I.H.; Von Doenhoff, A.E. *Theory of Wing Sections Including a Summary of Airfoil Data*; Courier Corporation: North Chelmsford, MA, USA, 1949.
28. Ramirez, A.S.; Marcos, M.E.I.; Haro, F.B.; D'Amato, R.; Sant, R.; Porras, J. Application of FDM technology to reduce aerodynamic drag. *Rapid Prototyp. J.* **2019**, *25*, 781–791. [CrossRef]
29. Szwedziak, K.; Łusiak, T.; Bąbel, R.; Winiarski, P.; Podsędek, S.; Doležal, P.; Niedbała, G. Wind Tunnel Experiments on an Aircraft Model Fabricated Using a 3D Printing Technique. *J. Manuf. Mater. Process.* **2021**, *6*, 12. [CrossRef]